PHYSICAL REVIEW B **91**, 245134 (2015)

Unified theory of spiral magnetism in the harmonic-honeycomb iridates α, β, and γ Li_2IrO_3

Itamar Kimchi,[1] Radu Coldea,[2] and Ashvin Vishwanath[1,3]
[1]*Department of Physics, University of California, Berkeley, California 94720, USA*
[2]*Clarendon Laboratory, University of Oxford, Parks Road, Oxford OX1 3PU, United Kingdom*
[3]*Materials Science Division, Lawrence Berkeley National Laboratories, Berkeley, California 94720, USA*

(Received 28 August 2014; revised manuscript received 19 May 2015; published 15 June 2015)

A family of insulating iridates with chemical formula Li_2IrO_3 has recently been discovered, featuring three distinct crystal structures α,β,γ (honeycomb, hyperhoneycomb, stripyhoneycomb). Measurements on the three-dimensional polytypes, β- and γ-Li_2IrO_3, found that they magnetically order into remarkably similar spiral phases, exhibiting a noncoplanar counter-rotating spiral magnetic order with equivalent $q = 0.57$ wave vectors. We examine magnetic Hamiltonians for this family and show that the same triplet of nearest-neighbor Kitaev-Heisenberg-Ising (KJI) interactions reproduces this spiral order on both β- and γ-Li_2IrO_3 structures. We analyze the origin of this phenomenon by studying the model on a one-dimensional zigzag chain, a structural unit common to the three polytypes. The zigzag-chain solution transparently shows how the Kitaev interaction stabilizes the counter-rotating spiral, which is shown to persist on restoring the interchain coupling. Our minimal model makes a concrete prediction for the magnetic order in α-Li_2IrO_3.

DOI: 10.1103/PhysRevB.91.245134 PACS number(s): 75.10.Jm, 75.10.Dg, 75.25.−j, 75.30.Et

Edge-sharing oxygen octahedra coordinating Ir^{4+} ions can exhibit unconventional magnetic interactions between the Ir $S_{\mathrm{eff}} = 1/2$ pseudospins. Strong spin-orbit coupling in iridium, which produces these low energy Kramer's doublets, can combine with 90° Ir-O-Ir exchange pathways to generate bond-dependent couplings identical to those discussed by Kitaev [1], as has been proposed in Refs. [2,3] for Na_2IrO_3. The collinear antiferromagnetic magnetism [4–7] later found in Na_2IrO_3 is distinct from simple Néel order, but can be captured by various models with or without Kitaev-type spin anisotropies [7–19]. The isostructural compound α-Li_2IrO_3, in which Ir forms separated layers of the two-dimensional (2D) honeycomb lattice, is available only in powder form. Thermodynamic and susceptibility measurements suggest it also orders magnetically [8], and powder neutron diffraction experiments found a magnetic Bragg peak with a small nonzero wave vector inside the first Brillouin zone [20], stimulating theoretical models [21,22] of spiral orders.

In the past two years, compounds with chemical formula Li_2IrO_3 have been successfully synthesized in two additional crystal structures (Fig. 1). In γ-Li_2IrO_3 the Ir sites form the three-dimensional (3D) stripyhoneycomb lattice [23,24] (space group #66 *Cccm*), featuring hexagons which are arranged in honeycomb strips of alternating orientation. In β-Li_2IrO_3 the Ir sites form the 3D hyperhoneycomb lattice [25,26] (space group #70 *Fddd*), featuring ten-site decagons which are reminiscent of the hyperkagome [27] lattice of $Na_4Ir_3O_8$. The relation between these structures is captured by their designation as harmonic-honeycomb iridates [23,28], a structural series in which α-, β-, γ-Li_2IrO_3 are labeled by $n = \infty,0,1$, respectively. Common features include local threefold coordination of sites, as well as identical 2D projections along the $\boldsymbol{a}$ and $\boldsymbol{b}$ parent orthorhombic axes; the $\boldsymbol{c}$ axis projections are distinct.

Recent experiments using resonant magnetic x-ray diffraction have successfully determined the magnetic ordering in β- and γ-Li_2IrO_3 single crystals [24,26]. The results are striking. Both compounds order into a complex spiral at a temperature $T_N = 38$ K. This order hosts counter-rotating spirals within the unit cell, exhibiting a particular pattern of noncoplanar tilts. The spiral wave vector $\boldsymbol{q}$ lies along the orthorhombic $\boldsymbol{a}$ axis, with the same apparently incommensurate magnitude $q = 0.57(1)\times 2\pi/a = 0.61(1)$ Å^{-1} in both structures. Except for the angle of the noncoplanar tilt, the magnetic orders observed in β- and γ-Li_2IrO_3 are equivalent to each other, though occurring in different lattice settings.

In this work we analyze the origin of this phenomenon by theoretically studying the three Li_2IrO_3 systems at the level of lattice magnetic Hamiltonians. We show that a microscopically derivable set of nearest-neighbor interactions, consisting of Kitaev, Heisenberg, and Ising exchanges, is sufficient for capturing the observed spiral magnetic order. This Hamiltonian is

$$H = \sum_{\langle ij\rangle} \left[K\, S_i^{\gamma_{ij}} S_j^{\gamma_{ij}} + J\, \vec{S}_i \cdot \vec{S}_j + I_c\, S_i^{r_{ij}} S_j^{r_{ij}} \right], \tag{1}$$

where K is the Kitaev coupling, and I is a distinct Ising coupling of the spin components parallel to the bond orientation, i.e., $S^{r_{ij}} \equiv \vec{S} \cdot \hat{r}_{ij}$, where $\hat{r}_{ij} = (\vec{i}-\vec{j})/|i-j|$ is the unit vector from site i to site j (see the Appendix including Fig. 4 for details). In this model the Ising term I_c is chosen to be active only on those symmetry-distinguished bonds which are parallel to the $\boldsymbol{c}$ axis, where it becomes $I_c S_i^c S_j^c$. For the Kitaev coupling of spin component γ_{ij}, the bond-dependent axis $\gamma_{ij} \in (x,y,z)$ is the Ir-O unit vector from iridium site i to one of the oxygens in its coordinating octahedron, uniquely chosen so that γ_{ij} is perpendicular to r_{ij} or, equivalently, perpendicular to the bond's $Ir_iO_2Ir_j$ square. Here $\hat{z} = \hat{b}$ and $\hat{x},\hat{y} = (\hat{a}\pm\hat{c})/\sqrt{2}$. As is clear from this representation, the three different exchanges K,J,I are all symmetry allowed and can be microscopically generated [29] already in the limit of cubic O_6 octahedra.

The phase diagram of Eq. (1), shown in Fig. 2(a), exhibits a remarkable feature. The experimentally observed spiral order in the β and γ lattices is stabilized in our theoretical model as the ground state on all three lattices, for certain parameters such as $(K,J,I_c) = (-12,0.6,-4.5)$ meV. Moreover, the

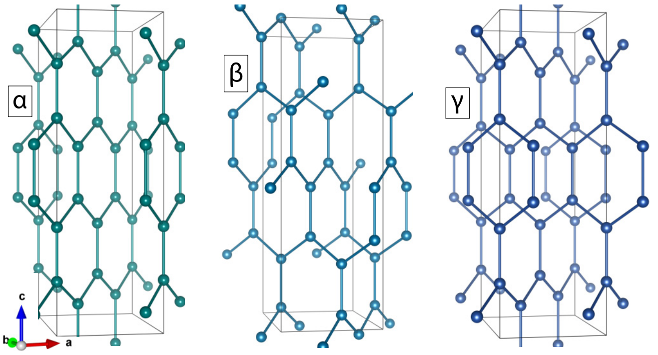

FIG. 1. (Color online) Lattices of Ir in α-, β-, γ-Li$_2$IrO$_3$, with parent orthorhombic a,b,c axes. Experiments on the 3D lattices, β- and γ-Li$_2$IrO$_3$, found strikingly similar spiral orders.

surrounding phase diagrams, computed (see details below) by setting Eq. (1) on each of the three α-, β-, γ-Li$_2$IrO$_3$ lattices, are all quite similar. In Fig. 2 the phase diagrams on α,β,γ lattices are shown for the same parameter range, permitting this visual comparison. This feature suggests that the experimental observations, of the striking similarity between the β- and γ-Li$_2$IrO$_3$ spiral orders, may be captured within this effective $S = 1/2$ Hamiltonian with nearest-neighbor exchanges.

To understand the striking similarity between the Fig. 2 phase diagrams found in our numerical computations on the different lattices, we introduce a conceptual toy model consisting of a one-dimensional (1D) zigzag chain. This minimal conceptual model may be motivated as follows. Observe that the symmetries of the Li$_2$IrO$_3$ polytypes single out the set of Ir-Ir bonds which lie parallel to the crystallographic $\boldsymbol{c}$ axis. These c bonds, with $r_{ij} = c$, all carry Kitaev couplings of $\gamma_{ij} = z = b$. The remaining "d bonds" (as well as their $\gamma_{ij} = x,y$) all lie diagonal to the a,b,c axes. This symmetry-enforced distinction suggests the microscopic mechanisms for setting $I_d = 0$ in Eq. (1). Now consider decomposing the Hamiltonian Eq. (1) into its interactions on c bonds and on d bonds, $H = H_c + H_d$. The d-bonds Hamiltonian H_d is then a sum of decoupled 1D zigzag chains at various positions and orientations, $H_d = \sum H_{1D}$, turning all three lattices into sums over identical H_{1D} building blocks.

Zigzag-chain minimal model. The zigzag-chain toy model is a conceptual mechanism for connecting the full numerical computations. Its solution is transparent, clarifying how essentially the same form of spiral order arises from Eq. (1) on the distinct 3D lattices. We complement its analytical insight by numerically computing the phase diagrams as we mathematically interpolate between the 3D lattices: even as we smoothly turn off the interchain bonds, reducing the 3D lattices to the 1D chain, the spiral phase remains stable.

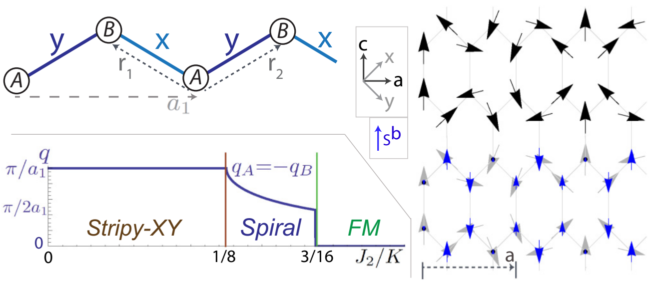

FIG. 3. (Color online) Zigzag chain and spiral. As evident in this 1D minimal model for the Li$_2$IrO$_3$ lattices (top left), the counter-rotating coplanar spiral order can be stabilized by Kitaev interactions within the coplanar ansatz Eq. (3) (bottom left; here with $K < 0$, $J = |K|/3$). For each lattice, restoring the interchain couplings preserves the counter-rotating S^a,S^c spiral (top right), while also introducing noncoplanar S^b components (overlayed in blue, bottom right). Together they form the experimentally observed order.

Since we define H_{1D} by dropping the interchain c bonds, here we mitigate the loss of the I_c exchange by introducing a second-neighbor Heisenberg J_2 interaction. This J_2 can be discarded when the full 3D lattice is restored. The zigzag-chain geometry is defined in Fig. 3; let r_1,r_2 point from an A-sublattice site to its neighboring B sites, and choose the 1D Bravais lattice with vector $a_1 = r_2 - r_1$ so that the A sites lie at integer positions $r = na_1$. The single-chain Hamiltonian is

$$\begin{aligned} H_{1D} = \sum_{r=na_1} \big[& K\left(S^x_{A,r}\, S^x_{B,r+r_1} + S^y_{A,r}\, S^y_{B,r+r_2}\right) \\ & + J\left(\vec{S}_{A,r}\cdot\vec{S}_{B,r+r_1} + \vec{S}_{A,r}\cdot\vec{S}_{B,r+r_2}\right) \\ & + J_2\left(\vec{S}_{A,r}\cdot\vec{S}_{A,r+a_1} + \vec{S}_{B,r-r_2}\cdot\vec{S}_{B,r+r_1}\right)\big]. \qquad (2) \end{aligned}$$

In the following we consider the x,y coplanar spiral magnetic orders that could be stabilized by the 1D minimal model Eq. (2), with spin ordering confined to the x,y (or equivalently

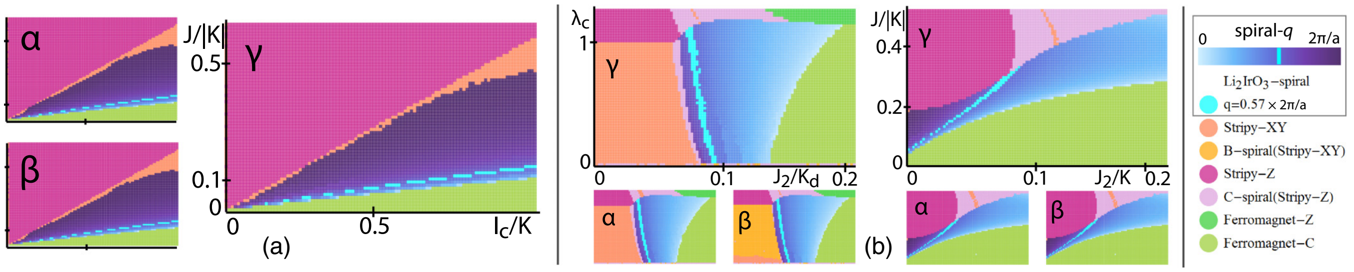

FIG. 2. (Color online) Phase diagrams on α-, β-, γ-Li$_2$IrO$_3$. In the vicinity of the spiral phase (shaded blue) which contains the experimentally observed magnetic order, the semiclassical phase diagrams appear remarkably similar across the α-, β-, γ-Li$_2$IrO$_3$ lattices. (a) The nearest-neighbor KJI_c model ($J_2 = 0$) is sufficient for capturing the observed spiral, and exhibits this cross-lattice similarity. (b) (Left) the spiral from the 1D zigzag chain model persists to the full lattices; (right) taking $J_2 \to 0$ requires large $|K|/J$; see parameters below. For the 2D α polytype, shading indicates the equivalent spiral $\boldsymbol{q}$ along $\boldsymbol{a}$ as described in the text.

a,c) plane. (Restoring the interchain z-type Kitaev couplings will produce the noncoplanar tilt.) First consider Eq. (2) at the exactly solvable point $J_2 = 0$, $K = -2J$, $K < 0$, where a site-dependent spin rotation [3,30,31] exposes it as a Heisenberg ferromagnet in a rotated basis. Its exact quantum ground state is a *stripy* collinear antiferromagnet (AFM) of the original spins. Now perturbing around this point by taking J smaller than $|K|/2$, the ground state has Stripy-XY antiferromagnetic order, with ordered spins collinear along S^x/S^y which are aligned on x/y-type bonds and anti-aligned along y/x-type bonds. Focusing on large FM $K < 0$ with small AF $J > 0$ satisfying $K + 2J < 0$, we expect the zigzag chain model to capture states which are x,y coplanar.

Switching on J_2 frustrates the stripy order. Focusing on the scenarios where the ordered spins remain confined to the x,y plane, we conceptually consider below a general spiral order with the ansatz,

$$\left(S^x_{s,r}, S^y_{s,r}\right) = (\mathrm{Re},\mathrm{Im})[\exp\{-i(q_s r + \phi_s)\}] \qquad (3)$$

where the sublattice index s takes the values $\{A,B\}$, and the two sublattices have spiral wavevectors $q_A = \pm q_B$ and phases ϕ_A,ϕ_B.

Consider the case of counter-rotation, $q_B = -q_A = \theta/a_1$ with $\theta > 0$ (a_1 is defined in Fig. 3). The energy per unit cell is given by

$$E_-(\theta) = K \sin(\theta/2)\sin(\phi_A + \phi_B) + 2J_2\cos(\theta). \qquad (4)$$

Minimizing the energy with respect to the sublattice phases (for $K < 0$) immediately fixes their sum to be $\phi_A + \phi_B = \pi/2$. Now consider the minimization with respect to the spiral rotation angle θ. There are three cases. (1) For small $|J_2|$, Eq. (4) is minimized at $\theta = \pi$, producing the stripy-XY AFM state, with energy $E_{\mathrm{stripy}} = K - 2J_2$. (2) For larger ferromagnetic $J_2 < 0$, a global minimum develops at an incommensurate wave vector fixed by $\sin(\theta/2) = K/(8J_2)$, for $|J_2| > |K|/8$. This incommensurate counter-rotating spiral phase has energy $E_{\mathrm{spiral}} = 2J_2 + K^2/(16J_2)$. (3) At larger $|J_2|$ it gives way to the $q = 0$ ferromagnet solution ($\phi_A = \phi_B$) with energy $E_{\mathrm{FM}} = K + 2J + 2J_2$. The phase diagram as well as the associated wavevector q, which result from this computation with the coplanar ansatz Eq. (3), are shown in Fig. 3.

It is also evident that a mostly Heisenberg model cannot produce a counter-rotating spiral. This is true even if it is supplemented by, e.g., Dzyaloshinskii-Moriya couplings. To see this, examine the generic spin correlations of the ansatz state Eq. (3). Between neighboring sites $i = (A,r)$ and $j = (B,r+v)$, they are

$$\left\langle S^x_i S^x_j \pm S^y_i S^y_j \right\rangle = \delta(q_B \mp q_A)\cos(q_B v + \phi_B \mp \phi_A). \qquad (5)$$

The upper sign gives the usual Heisenberg correlations, while the lower sign corresponds to the spin-anisotropic correlations of the Kitaev exchange. The δ-function factor ensures that the Heisenberg/Kitaev correlations vanish in the counter/co-rotating spiral, respectively.

Noncoplanar spiral from coupled chains. Each of the three α-, β-, γ-$\mathrm{Li_2IrO_3}$ lattices is reached from the decoupled-chains limit by introducing a particular pattern of interchain couplings between chains of various positions and orientations. We find that these interchain couplings both help to stabilize the coplanar spiral found in the 1D model, and also introduce an alternating pattern of noncoplanar tilts in the rotation planes of successive zigzag chains, as follows. By taking Eq. (3) with appropriate phases and introducing the $\langle S^b\rangle$ component, we describe the full spiral by

$$\vec{S}_{s,r} = \cos(q_s r_a)\langle S^c\rangle \hat{c} - \sin(q_s r_a)(\langle S^a\rangle \hat{a} \pm \langle S^b\rangle \hat{b}), \qquad (6)$$

with $q_B = -q_A = q > 0$ denoting counter-rotation between upper ($s = B$) and lower (A) sites on each zigzag chain. The $\pm$ sign alternates between successive zigzag chains, tilting S^a towards $\pm S^b$, with magnitudes satisfying $\langle S^a\rangle^2 + \langle S^b\rangle^2 = \langle S^c\rangle^2$ required by the constraint of fixed length spin on each site. This tilting is stabilized energetically by the strong $K_c S^b_i S^b_j$ interchain coupling, and its alternating pattern is set by $J_c > 0$. The resulting noncoplanar spiral is composed of a coplanar spiral in each zigzag chain, whose plane of rotation alternates in orientation between adjacent zigzag chains. Figure 3 shows the resulting spiral as viewed in the b-axis projection common to the lattices, for parameters with $q = 0.57 \times 2\pi/a$.

Applicability of the 1D model. We demonstrate the applicability of the 1D model to the physical lattices, by studying the smooth evolution of each lattice to its decoupled-chains limit. In particular, we introduce an interchain coupling coefficient λ_c, and map the semiclassical phase diagram of $H_\lambda = \lambda_c H_c + H_d$. Here the Hamiltonian Eq. (1) is supplemented by the J_2 exchange between second neighbors of the Ir lattice, on the two intrachain bonds [as in Eq. (2)] as well as on the four remaining bonds (where it is suppressed by the interchain coupling coefficient λ_c). Such a study is shown in Fig. 2(b), showing the phase diagram as a function of λ_c and J_2 for $K_d = 0.8K_c$, $J_c = 2J_d = |I_c|, I_c = K_c/3$. These parameters, though not likely to be physically relevant, allow this mathematical interpolation from 3D to 1D. We find that the spiral phase remains stable from the 1D limit $\lambda_c = 0$ through the isotropic physical lattice $\lambda_c = 1$, on each of the lattices.

Necessity of strong Kitaev interactions. We consider a KJI_c–J_2 Hamiltonian, such as the model we previously reported [24] for the spiral order in γ-$\mathrm{Li_2IrO_3}$, and attempt to tune $J_2 \to 0$ while preserving the experimentally observed spiral phase. Such a study is presented in Fig. 2(b), showing the phase diagram in $J/|K|$ and J_2/K, here for $I_c/K = 0.375$. We find that to discard the second neighbor interactions, the ratio $|K|/J$ must simultaneously be taken to be quite large ~ 20. One representative such set of nearest-neighbor couplings is $(K,J,I_c) = (-12, 0.6, -4.5)$ meV. Here the overall scale is set so that the mean field ordering temperature $T_N = 40$ K matches the experimental T_N. Putting aside the Ising term, this ratio $J/|K| = 0.05$ lies well within the 2D Kitaev quantum spin liquid phase on the honeycomb lattice [3,11,32], though it may lie outside the 3D quantum spin liquid phases on the 3D lattices [28].

Semiclassical solutions. The semiclassical approximation which we employ can capture incommensurate spiral orders as well as other magnetic phases. We represent spins by unconstrained vectors, yielding a quadratic Hamiltonian which is appropriate for capturing fluctuating states with small ordered moments. The lowest energy mode of this quadratic Hamiltonian is associated with the ordering instability of the spin model, and is straightforwardly found by Fourier transform. This is expected to be the leading ordering instability out of a high temperature paramagnetic phase assuming a continuous transition. Potentially quantum fluctuations could play a similar role. Our phase diagrams outline the evolution of this leading instability.

The algorithmically generated phase diagrams in Fig. 2 host the Li_2IrO_3 spiral phase as well as various competing orders. These include stripy antiferromagnets, where spins of the given component are aligned only along that Kitaev bond type; incommensurate orders with q vectors along $\boldsymbol{b}$ or $\boldsymbol{c}$, which retain stripylike correlations within the unit cell; and ferromagnets with S^c or S^z alignment.

Coplanar and tilt modes. The experimentally observed spiral phase in the β and γ lattices, expressed in Eq. (6) and plotted in Fig. 3, was identified numerically in two steps. Observe that the noncoplanar S^b tilt pattern is distinguished from the S^a, S^c coplanar spiral order by a mirror eigenvalue, associated with a $\boldsymbol{c}$-axis reflection. The coplanar spiral is mirror-even while the tilt mode is mirror-odd. Indeed we find that they appear as distinct modes in the Fourier transform of Hamiltonians in the spiral phase. The global ground state is numerically found to be the coplanar spiral mode, which furthermore is found to exhibit $\langle S^a \rangle < \langle S^c \rangle$. Nonlinear effects above our quadratic approximation, which would tend to force the length of spin to be similar across sites, are likely to mix this solution with an additional mode. We adopt the following heuristic approach to include effects of nonlinearity which become more important with growing magnitude of the order parameter. We examine the lowest energy excited mode available for this mixing, and find throughout that it consists of the experimentally observed $\langle S^b \rangle$ tilt pattern. While the instability analysis provides us a phase diagram that includes an incommensurate spiral, a more controlled calculation of nonlinear effects is required to decide whether the observed magnetic order appears or some other state is favored in this regime of parameters for the quantum $S = 1/2$ Hamiltonian.

This analysis fixes the pattern of noncoplanar tilts. Their rough magnitude (though not their overall sign) can be estimated by constructing a fully classical configuration from the two mixing modes. For the values $(K, J, I_c) = (-12, 0.6, -4.5)$ meV, the resulting tilt angle is 63°, similar to the angles observed experimentally, 42° and 55°; it can be tuned through these values by varying the relative ratios of the exchange parameters. However, we expect fluctuations to be relevant for these systems. Indeed, in the experimentally determined magnetic structures [24,26] of β- and γ-Li_2IrO_3, the extracted ordered magnetic moment is not constant in magnitude between sites, but it is smaller by 10%–20% when it is aligned in the ab plane compared to when it is pointing along the c axis. This variation is likely due to a combination of g factor anisotropies and quantum fluctuations of these $S = 1/2$ moments.

Zigzag-chain mechanism in α-Li_2IrO_3. α-Li_2IrO_3 [33] has a layered structure of stacked 2D iridium honeycombs separated by layers of Li ions. For comparison with the other lattices we construct an orthorhombic parent unit cell of the same size as for the β and γ structures (see the Appendix for details) where the honeycombs are in the $(\boldsymbol{a} + \boldsymbol{b}, \boldsymbol{c})$ plane (Fig. 1). The Hamiltonian Eq. (1) predicts an incommensurate spiral order in the honeycomb layers with the same pattern of counter-rotation between adjacent sites and noncoplanarity between vertical (c-axis) bonds as in the β and γ lattices. Remarkably, the energetics is such that for the same values of the exchange parameters (K, J, I), the calculated relative angles of spins on nearest-neighbor sites is the same on all three lattices.

In particular, energetic analysis of the (K, J, I) model Hamiltonian on the α-Li_2IrO_3 lattice, with parameters chosen to reproduce the experimentally observed order on β- and γ-Li_2IrO_3, predicts a magnetic structure where the relative spin orientations between adjacent sites are the same as in the β and γ polytypes. This implies that the projection of the α-Li_2IrO_3 ordering wave vector onto the honeycomb layers is $q_{1D} = q \cos\theta$, where $q = 0.57 * 2\pi/a$ is the propagation vector magnitude in the β and γ lattices, and $\theta = \cos^{-1}(a/\sqrt{a^2 + b^2})$ is the angle between the $\boldsymbol{a}$ axis and the α-Li_2IrO_3 honeycomb layers. Here the subscript 1D emphasizes that for a given honeycomb plane, the spiral wave vector lies along a zigzag chain, as in the 1D model of decoupled chains [Eq. (2) and Fig. 3].

The resulting value for this projection, $q_{1D} \sim 0.35$ Å^{-1}, serves as an estimated lower bound for the magnitude of the 3D ordering wave vector $\boldsymbol{q}_{3D}$ that would occur in the real material. Weak interlayer couplings can give $\boldsymbol{q}_{3D}$ a finite component normal to the honeycomb layers, suggesting a possible range for the magnitude $|\boldsymbol{q}_{3D}|$. Future experiments on α-Li_2IrO_3 single crystal samples could test these predictions for $\boldsymbol{q}_{3D}$, as well as the predictions for noncoplanarity and counter-rotation, which are highly nontrivial features for the magnetic order on a honeycomb lattice. In particular the noncoplanarity would break the C centering of the honeycomb lattice, leading to a doubling of the primitive unit cell; this is a rather unusual feature for spiral order, and distinct from other theoretical models [21,22] for α-Li_2IrO_3.

Conclusion. The experimental observations in β- and γ-Li_2IrO_3 are intriguing: the two compounds undergo a magnetic ordering transition, at similar temperatures, into an unusual spiral magnetic order, with spiral wave vectors which are the same up to the experimental accuracy. This spiral wave vector appears to be incommensurate, with no clear mechanism for strong lattice pinning. In this work we have found a nearest-neighbor magnetic Hamiltonian which reproduces the complete symmetry of the spiral magnetic order on the two lattices including the pattern of counter-rotation and noncoplanarity. The origin of this cross-lattice similarity is clarified by a 1D zigzag-chain minimal model. This transparent model is sufficiently minimal to be a common building block for the lattices, yet sufficiently complex to stabilize the counter-rotating spiral order. Its applicability is verified by smoothly extending it towards the physical lattices, and its predictions for α-Li_2IrO_3 are testable. The apparent commonality across the Li_2IrO_3 family suggests that to capture certain aspects of the magnetism, it may be sufficient to describe the different compounds via the same low-energy effective Hamiltonian. Why this may happen remains to be understood.

Note added. During publication of this paper, a preprint [34] has appeared which discusses magnetism on the β- and γ-Li_2IrO_3 lattices. One of the magnetic spiral phases identified there correctly captures the magnetic structure observed [26] in β-Li_2IrO_3. However, that phase, as well as the other spiral phases found in that work, differ in detail (symmetry of the ordering pattern) [35] from the spiral phase discussed here and observed experimentally [24] for γ-$\mathrm{Li_2IrO_3}$.

Acknowledgments. We thank James Analytis for previous collaborations. This work was supported by the Director, Office of Science, Office of Basic Energy Sciences, Materials Sciences and Engineering Division, of the U.S. Department of Energy under Contract No. DE-AC02-05CH11231. R.C. acknowledges support from EPSRC (U.K.) through Grant No. EP/H014934/1.

APPENDIX

1. Parent orthorhombic setting for α-, β-, γ-$\mathrm{Li_2IrO_3}$

In this Appendix we define simple idealizations of the Ir lattices in the crystals, by taking oxygen octahedra to have ideal cubic symmetry. This provides a pedagogically clearer description of the 3D lattices. For the layered α-$\mathrm{Li_2IrO_3}$ monoclinic structure, our definition of parent orthorhombic axes is a key step in our prediction of its magnetic order, as discussed in the text.

We use a coordinate system based on the parent orthorhombic axes shown in Fig. 1. These vectors, which are the conventional crystallographic axes for β- and γ-$\mathrm{Li_2IrO_3}$, are related to the Ir-O x,y,z axes by

$$\boldsymbol{a} = (2,2,0), \quad \boldsymbol{b} = (0,0,4), \quad \boldsymbol{c} = (6,-6,0). \tag{A1}$$

In the equation above we have written the a,b,c vectors in terms of the Cartesian (cubic orthonormal) x,y,z coordinate system. The $\hat{x},\hat{y},\hat{z}$ lattice vectors in this coordinate system are defined as the vectors from an iridium atom to its neighboring oxygen atoms in the idealized cubic limit, with the unit of length being the Ir-O distance. Nearest neighbor bonds in the resulting Ir lattice have length $\sqrt{2}$, and second neighbors are at distance $\sqrt{6}$.

For each lattice, we express its Bravais lattice vectors, as well as each of its sites of its unit cell, in terms of the a,b,c axes. A given vector or site, written as (n_a,n_b,n_c), is converted to the Cartesian coordinate system by $(n_x,n_y,n_z) = n_a\boldsymbol{a} + n_b\boldsymbol{b} + n_c\boldsymbol{c}$. The conventional unit cell in the orthorhombic setting, which contains 16 sites, is found by combining the primitive unit cell with the Bravais lattice vectors.

β-$\mathrm{Li_2IrO_3}$ *hyperhoneycomb* lattice ($n = 0$ harmonic honeycomb), space group $Fddd$ (#70):

Primitive unit cell (four sites):

$$(0,0,0); \quad \left(0,0,\tfrac{1}{6}\right); \quad \left(\tfrac{1}{4},\tfrac{-1}{4},\tfrac{1}{4}\right); \quad \left(\tfrac{1}{4},\tfrac{-1}{4},\tfrac{5}{12}\right). \tag{A2}$$

Bravais lattice vectors (face centered orthorhombic):

$$\left(\tfrac{1}{2},\tfrac{1}{2},0\right); \quad \left(\tfrac{1}{2},-\tfrac{1}{2},0\right); \quad \left(\tfrac{1}{2},0,\tfrac{1}{2}\right). \tag{A3}$$

γ-$\mathrm{Li_2IrO_3}$ *stripyhoneycomb* lattice ($n = 1$ harmonic honeycomb), space group $Cccm$ (#66):

Primitive unit cell (eight sites):

$$\begin{gathered}(0,0,0); \quad \left(0,0,\tfrac{1}{6}\right); \quad \left(\tfrac{1}{4},\tfrac{-1}{4},\tfrac{1}{4}\right); \quad \left(\tfrac{1}{4},\tfrac{-1}{4},\tfrac{5}{12}\right);\\ \left(0,0,\tfrac{1}{2}\right); \quad \left(0,0,\tfrac{2}{3}\right); \quad \left(\tfrac{1}{4},\tfrac{1}{4},\tfrac{3}{4}\right); \quad \left(\tfrac{1}{4},\tfrac{1}{4},\tfrac{11}{12}\right).\end{gathered} \tag{A4}$$

Bravais lattice vectors (base centered orthorhombic):

$$\left(\tfrac{1}{2},\tfrac{1}{2},0\right); \quad \left(\tfrac{1}{2},-\tfrac{1}{2},0\right); \quad (0,0,1). \tag{A5}$$

α-$\mathrm{Li_2IrO_3}$ *layered honeycomb* lattice ($n = \infty$ harmonic honeycomb), space group $C2/m$ (#12).

To discuss the layered honeycomb α-$\mathrm{Li_2IrO_3}$ polytype within the context of its 3D cousins, we must first set up a single global coordinate system. The two 3D lattices are captured, up to minute distortions, by the same parent simple-orthorhombic coordinate system of a,b,c axes.

The α polytype however has monoclinic symmetry and is conventionally described by a set of monoclinic axes, which we denote $\boldsymbol{a_m},\boldsymbol{b_m},\boldsymbol{c_m}$. The parent orthorhombic $\boldsymbol{a},\boldsymbol{b},\boldsymbol{c}$ axes defined above are distinct from the conventional monoclinic axes used to describe this $C2/m$ crystal. Here we define an orthorhombic coordinate system from a higher-symmetry idealization of these monoclinic axes, by taking $\boldsymbol{a_o} = \boldsymbol{a_m} + \boldsymbol{c_m}$, $\boldsymbol{b_o} = \boldsymbol{a_m} - \boldsymbol{c_m}$, $\boldsymbol{c_o} = \boldsymbol{2b_m}$. The a_o,b_o,c_o notation here signifies that, up to the distortions of oxygen octahedra, the resulting a,b,c axes are identical to the orthorhombic axes of the β and γ polytypes. This higher-symmetry idealization consists of the approximation that $|a_m| = |c_m|$, which is wrong in the physical lattice [33] only by about 1%. The transformation between the conventional monoclinic axes and the universal orthorhombic axes is also described by the coordinate notation as

$$\boldsymbol{a_m} = \left(\tfrac{1}{2},\tfrac{1}{2},0\right); \quad \boldsymbol{b_m} = \left(0,0,\tfrac{1}{2}\right); \quad \boldsymbol{c_m} = \left(\tfrac{1}{2},-\tfrac{1}{2},0\right). \tag{A6}$$

The a,b,c coordinate system preserves the key features used to discuss the other lattices, namely that bonds lying along the c axis carry Kitaev coupling $b = z$, while remaining bonds are diagonal to the a,b,c axes and form the d-bonds zigzag chains. Equivalently, we choose a right handed orthorhombic coordinate system, with the c axis as the unique axis along which one third of Ir-Ir bonds are aligned, and the b axis as the unique axis along which one third of Ir-O bonds are aligned.

Primitive unit cell (two sites, denoted A and B):

$$(0,0,0); \quad \left(\tfrac{1}{4},-\tfrac{1}{4},\tfrac{1}{12}\right). \tag{A7}$$

Bravais lattice vectors, here denoted as a_1,a_2,a_3:

$$a_1 = \left(\tfrac{1}{2},-\tfrac{1}{2},0\right); \quad a_2 = \left(-\tfrac{1}{4},\tfrac{1}{4},\tfrac{1}{4}\right); \quad a_3 = \left(\tfrac{1}{2},\tfrac{1}{2},0\right), \tag{A8}$$

where the first two vectors span the 2D honeycomb plane. These vectors are all of the same length ($\sqrt{6}$ in units of Ir-O distance), and span the six second neighbors within a honeycomb plane, plus one of the two additional pairs of sites on adjacent planes which are at the same distance, given by vectors $\pm a_3 = \pm(\hat{x} + \hat{y} + 2\hat{z})$ (the remaining pair belongs to the opposite sublattice).

Within a honeycomb plane, the nearest neighbor vectors from A to B are r_1,r_2,r_3, with $r_3 = -r_1 - r_2$ and

$$r_1 = \left(-\tfrac{1}{4},\tfrac{1}{4},\tfrac{1}{12}\right); \quad r_2 = \left(\tfrac{1}{4},-\tfrac{1}{4},\tfrac{1}{12}\right). \tag{A9}$$

The Bravais vectors above are related by $a_1 = r_2 - r_1$, $a_2 = r_1 - r_3$. For reference we also note these Ir-Ir vectors in the Ir-O coordinate system, $r_1 = -\hat{y} + \hat{z}$, $r_2 = \hat{x} - \hat{z}$, $r_3 = -\hat{x} + \hat{y}$. This immediately implies that the Kitaev labels for (r_1,r_2,r_3) bonds are (x,y,z), respectively.

Zigzag chain as basic structural unit:

The 1D zigzag chain is composed of sites A and B,

$$(0,0,0); \quad \left(\tfrac{1}{4},-\tfrac{1}{4},\tfrac{1}{12}\right), \tag{A10}$$

together with a single (1D) Bravais lattice vector,

$$a_1 = \left(\tfrac{1}{2}, -\tfrac{1}{2}, 0\right). \tag{A11}$$

The reflection $b \to -b$ takes this zigzag chain to its symmetry-equivalent partner, in which the minus sign in the two equations above is replaced by a plus sign.

In this notation it is evident that the zigzag chains form the basic structural unit in all three Li_2IrO_3 polytypes. In each lattice, sites are naturally partitioned into pairs which match this zigzag chain unit cell, and each lattice contains the chain's Bravais lattice vector. The magnetic Hamiltonian on each lattice is constructed as the sum of zigzag-chain Hamiltonians plus interchain interaction terms.

2. Ising interactions

The Ising term defined in Eq. (1) is distinct from any combination of Kitaev and Heisenberg exchanges. (The geometry is visualized in Fig. 4.) It can be related to the "off-diagonal" symmetric interactions which have recently appeared in the literature [36–38] under the symbols Γ or D. For instance, if on a z bond one writes the term $+\Gamma(S_i^x S_j^y + S_i^y S_j^x)$, then the triplet KJI reproduces $JK\Gamma$ by setting $(K,J,I) = (K-\Gamma, J+\Gamma, -2\Gamma)$. The bond-Ising interaction may be preferred as its definition, unlike Γ, is independent of coordinate system.

In Eq. (1) we have included the Ising coupling only on c bonds, for the following reasons. First consider the coplanar spiral mode. Since $r_{ij} \perp \gamma_{ij}$ and on d bonds $\gamma_{ij} = (\hat{x},\hat{y})$, the d-bond r_{ij} take values $[(\hat{y},\hat{x}) \pm \hat{z}]/\sqrt{2}$, projecting I_d into a Heisenberg-Kitaev term when $\langle S^z \rangle = 0$. In contrast I_c couples spin component $\hat{c} = (\hat{x} - \hat{y})/\sqrt{2}$ and helps stabilize the spiral (Fig. 5). Second, we observe that the experimentally observed pattern of noncoplanar tilts is not favored by the d-bonds Ising exchange, whose r_{ij} orientations favor a different symmetry breaking pattern. The correct S^b tilts are instead stabilized by the K_c Kitaev term.

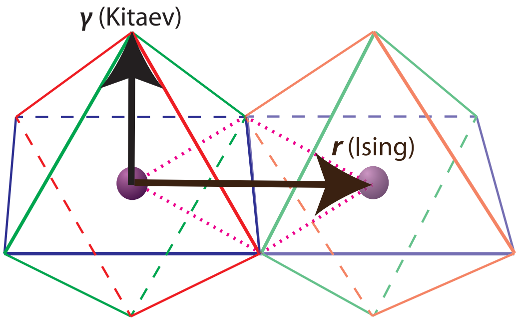

FIG. 4. (Color online) Visualization of geometry of Kitaev and Ising exchanges. The two neighboring Ir sites (purple spheres), with surrounding oxygens (vertices of octahedra), are shown. The oxygen octahedra of neighboring Ir sites are edge sharing in these structures. The axes for the anisotropic interaction terms are then determined as follows [see the discussion following Eq. (1) of the main text for details]. The Ising interaction axis $\vec{r}$ is the vector connecting the two Ir sites. The Kitaev interaction axis γ is perpendicular to the plane which contains r and the shared octahedra edge. For both interaction terms, the coupling axis for the quadratic spin interaction is defined as an axis with no orientation; here it is shown as an arrow (with an arbitrary direction of the arrow head) for ease of visualization.

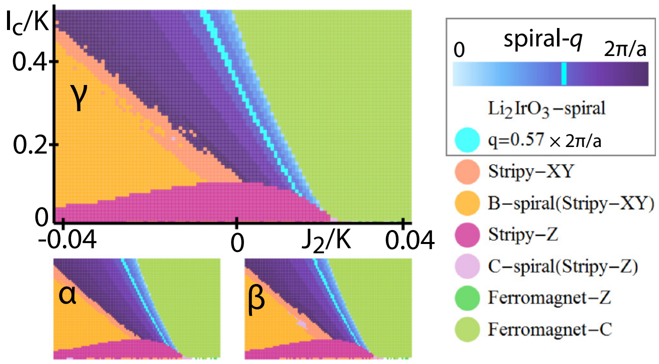

FIG. 5. (Color online) Here we observe that for $J = |K|/20$, finite $I_c < 0$ is required regardless of the sign or magnitude of J_2.

3. Details of relation between Ising and Γ terms

We show more explicitly how the off-diagonal symmetric interaction term, sometimes called the "Γ" exchange, can be made equivalent to the Ising term introduced above by appropriately modifying the strength of the Kitaev and Heisenberg couplings. This can be seen by writing the spin interaction matrix $J^{a,b}$ for the interaction $S^a J^{a,b} S^b$ (summation implied) of neighboring spins. Let us again write it in the KJI and $JK\Gamma$ notations for the interaction on a c bond, in the x,y,z basis,

$$\begin{pmatrix} \frac{1}{2}I_c + J & -\frac{1}{2}I_c & 0 \\ -\frac{1}{2}I_c & \frac{1}{2}I_c + J & 0 \\ 0 & 0 & K+J \end{pmatrix} \longleftrightarrow \begin{pmatrix} J & \Gamma_c & 0 \\ \Gamma_c & J & 0 \\ 0 & 0 & K+J \end{pmatrix}, \tag{A12}$$

where we have kept the c subscript on I_c and Γ_c to denote that these are the parameters for the c-type bond. The set of interaction matrices spanned by K,J,I is equivalent to that spanned by $J,K,\pm\Gamma$. In particular, our K,J,I_c model, with Ising interactions on c bonds, is related to a K,J,Γ_c model with off-diagonal Γ_c couplings on c bonds.

The bond-Ising interaction may be preferred for two reasons. First, its geometric definition, coupling the spin component along the Ir-Ir bond, is independent of coordinate system and thus free of sign ambiguities. In contrast, distinguishing $+\Gamma$ from $-\Gamma$ is coordinate dependent. This is most evident for the x and y bonds on the 3D lattices, where in the Γ notation the interaction appears with a positive sign on half of the x bonds and a negative sign on the remaining x bonds. In contrast, the Ising term directly sets the coupled spin component to the direction of the displacement vector between the two sites, and is invariant to the vector's sign. Second, the Ising coupling, of spin components along the bond, transparently indicates that this exchange is symmetry permitted even for ideal O_6 octahedra.

4. Details of the semiclassical solution

Here we give technical details for the semiclassical solution. First note that the 16-site unit cell of the orthorhombic axes contains four sites along the spiral propagation direction a; in contrast, the zigzag-chain 1D Bravais vector a_1 spans two sites. Hence a wave vector in units of π/a_1 is roughly analogous to one in units of $2\pi/a$.

For all three lattices, we use an eight-site unit cell with a base-centered orthorhombic Bravais lattice. In this choice of unit cell, the Brillouin zone is rotated (by 45 deg) and doubled in area from the BZ associated with the conventional orthorhombic coordinate system, e.g., it extends from $-2\pi/a$ to $+2\pi/a$ along the a axis. We perform numerical minimization by defining a $\pi/8$-spaced grid in the Brillouin zone and then using the constrained minimization algorithm of Broyden-Fletcher-Goldfarb-Shanno [39,40], independently starting at each grid point.

Let us write the explicit process of solution for the wave vector within the Fourier transform (FT). For concreteness we focus on the minimal parameters $(K,J,I_c) = (-12{,}0.6,-4.5)$ meV, on the β (hyperhoneycomb) lattice. This Hamiltonian is minimized at $\vec{q} = 0.57 \times 2\pi/|a| \times \hat{a}$. The FT ground state at this wave vector, energy -14.8 meV, has ordered spin moment $\vec{S} \propto \hat{c} \pm i0.48\hat{a}$, where the $\pm$ sign alternates between successive sites in the unit cells (shown above) when they are listed in order of their c coordinate. The second excited state at this wave vector, energy -12.1 meV, is capable of mixing with this ground state, and exhibits a wave function $\pm\hat{b}$ where this distinct $\pm$ symbol is chosen to give the same sign on two sites connected by a c bond, and opposite sign on two sites connected by a d bond; in other words, it alternates in pairs when sites are listed by their c coordinate. Observe that these definitions of sign structure are consistent with the definition of the wave function given in the text, Eq. (6).

The mixing mode energy can be tuned towards the ground state, for example in the nearby set of parameters with bond-strength anisotropy in the Kitaev term, $(K_c,K_d,J,I_c) = (-13.2,-11{,}0.6,-4.5)$ (in meV), the ground state coplanar mode has energy -13.8 meV, and the tilt mode is its first excited state, at energy -13.5 meV higher. This combined noncoplanar state is found on all three lattices. As discussed in the text, it agrees with the spiral order observed experimentally on both the β and the γ polytypes.

Finally, we note that in labeling the phases within the numerically computed phase diagrams, we have used features which are invariant across the phase, such as the ordering wave vector and the pattern across lattice sites. Due to the strong spin-orbit coupling which microscopically generates the model Hamiltonian, and the associated Hamiltonian-level breaking by the Kitaev as well as the Ising terms of any spin symmetries, the spin moment ordering direction on the Bloch sphere is not a robust measure of a phase. In particular, this Bloch sphere direction of the ordered spin moment generally varies smoothly as parameters are varied, within a given collinear antiferromagnetic or ferromagnetic phase.

5. Details of the 1D zigzag-chain solution

Here we present the full solution of the zigzag-chain model within the x,y-coplanar ansatz shown in the text. The quickest route to deriving the energy function Eq. (4) is to plug in the spin-spin correlations into the Hamiltonian Eq. (2). The nearest-neighbor correlations are given in Eq. (5); the second neighbor correlations are $\langle \vec{S}_r \cdot \vec{S}_{r+a_1} \rangle = \cos(qa_1)$. These two equations are sufficient for solving the model.

Alternatively, plugging in the ansatz Eq. (3) into the Hamiltonian Eq. (2) gives the following energy function:

$$\begin{aligned} E_{1\mathrm{D}} = \sum_{r=na_1} &[J_2[2\cos(\theta)] + K(\cos(\theta/2)\cos[f_-(r)] \\ &+ \sin(\theta/2)\sin[f_+(r)]) + J\{2\cos(\theta/2)\cos[f_-(r)]\}], \\ f_\pm(r) = [(&\phi_A \pm \phi_B) + r(q_A \pm q_B)]. \end{aligned} \tag{A13}$$

with $\theta = a_1 q_B$. Performing the average over 1D Bravais lattice sites $r = na_1$, we observe four possibilities. If $q_A = q_B \neq 0,\pi/a_1$, then the term with f_+ vanishes, while f_- are replaced by $(\phi_A - \phi_B)$. This co-rotating spiral is set by the interplay of primarily Heisenberg first and second neighbor exchanges, requires the typical geometrical frustration here encoded by J and J_2 of the same sign, and is the typical spiral one expects from frustrated Heisenberg models. If $q_A = -q_B \neq 0,\pi/a_1$, then the terms with f_- vanish, while f_+ are replaced by $(\phi_A + \phi_B)$. This is the counter-rotating spiral. The final possibilities are $\theta = \pm\pi$, leading to the stripy antiferromagnet, or $\theta = 0$, leading to the ferromagnet [in both cases $f_\pm$ are replaced by $(\phi_A \pm \phi_B)$], discussed above.

When studying the counter-rotating spiral, it is important to keep in mind the behavior of the phases under lattice translations. Due to the counter-rotation, here the *average* phase is the physical quantity; the arbitrary "overall phase" of the spiral, freely modified (for incommensurate q) by shifting r, is then the *difference* of phases $\phi_A - \phi_B$. We may choose the phases $\phi_A = \phi_B = \pi/4$ to satisfy $\phi_A + \phi_B = \pi/2$, keeping in mind that shifting the overall phase does not permit these phases to simultaneously be set to zero.

The stabilization of the spiral by Kitaev interactions can also be observed via Eq. (5) by fixing $\phi_A + \phi_B = \pi/2$. While the Heisenberg correlator vanishes, the spin component matching the Kitaev bond type exhibits nonzero correlations, $\langle S_r^x S_{r+r_1}^x \rangle_x = (1/2)\sin(\theta/2)$.

---

[1] A. Kitaev, Ann. Phys. **321**, 2 (2006).

[2] G. Jackeli and G. Khaliullin, Phys. Rev. Lett. **102**, 017205 (2009).

[3] J. Chaloupka, G. Jackeli, and G. Khaliullin, Phys. Rev. Lett. **105**, 027204 (2010).

[4] Y. Singh and P. Gegenwart, Phys. Rev. B **82**, 064412 (2010).

[5] X. Liu, T. Berlijn, W.-G. Yin, W. Ku, A. Tsvelik, Y.-J. Kim, H. Gretarsson, Y. Singh, P. Gegenwart, and J. P. Hill, Phys. Rev. B **83**, 220403 (2011).

[6] F. Ye, S. Chi, H. Cao, B. C. Chakoumakos, J. A. Fernandez-Baca, R. Custelcean, T. F. Qi, O. B. Korneta, and G. Cao, Phys. Rev. B **85**, 180403 (2012).

[7] S. K. Choi, R. Coldea, A. N. Kolmogorov, T. Lancaster, I. I. Mazin, S. J. Blundell, P. G. Radaelli, Y. Singh, P. Gegenwart, K. R. Choi, S.-W. Cheong, P. J. Baker, C. Stock, and J. Taylor, Phys. Rev. Lett. **108**, 127204 (2012).

[8] Y. Singh, S. Manni, J. Reuther, T. Berlijn, R. Thomale, W. Ku, S. Trebst, and P. Gegenwart, Phys. Rev. Lett. **108**, 127203 (2012).

[9] I. Kimchi and Y.-Z. You, Phys. Rev. B **84**, 180407 (2011).

[10] A. F. Albuquerque, D. Schwandt, B. Hetényi, S. Capponi, M. Mambrini, and A. M. Läuchli, Phys. Rev. B **84**, 024406 (2011).

[11] J. Chaloupka, G. Jackeli, and G. Khaliullin, Phys. Rev. Lett. **110**, 097204 (2013).

[12] R. Comin, G. Levy, B. Ludbrook, Z.-H. Zhu, C. N. Veenstra, J. A. Rosen, Y. Singh, P. Gegenwart, D. Stricker, J. N. Hancock, D. van der Marel, I. S. Elfimov, and A. Damascelli, Phys. Rev. Lett. **109**, 266406 (2012).

[13] K. Foyevtsova, H. O. Jeschke, I. I. Mazin, D. I. Khomskii, and R. Valentí, Phys. Rev. B **88**, 035107 (2013).

[14] I. I. Mazin, S. Manni, K. Foyevtsova, H. O. Jeschke, P. Gegenwart, and R. Valentí, Phys. Rev. B **88**, 035115 (2013).

[15] I. Mazin (private communication, 2014).

[16] B. H. Kim, G. Khaliullin, and B. I. Min, Phys. Rev. B **89**, 081109 (2014).

[17] H. Gretarsson, J. P. Clancy, X. Liu, J. P. Hill, E. Bozin, Y. Singh, S. Manni, P. Gegenwart, J. Kim, A. H. Said, D. Casa, T. Gog, M. H. Upton, H.-S. Kim, J. Yu, V. M. Katukuri, L. Hozoi, J. van den Brink, and Y.-J. Kim, Phys. Rev. Lett. **110**, 076402 (2013).

[18] H. Gretarsson, J. P. Clancy, Y. Singh, P. Gegenwart, J. P. Hill, J. Kim, M. H. Upton, A. H. Said, D. Casa, T. Gog, and Y.-J. Kim, Phys. Rev. B **87**, 220407 (2013).

[19] I. Rousochatzakis, U. K. Rössler, J. van den Brink, and M. Daghofer, arXiv:1209.5895, found noncoplanar vortex lattice orders in related models.

[20] R. Coldea, presentation at the MPI-Dresden workshop on Spin Orbit Entanglement (July 2013).

[21] J. Reuther, R. Thomale, and S. Rachel, Phys. Rev. B **90**, 100405 (2014).

[22] S. Nishimoto, V. M. Katukuri, V. Yushankhai, H. Stoll, U. K. Roessler, L. Hozoi, I. Rousochatzakis, and J. van den Brink, arXiv:1403.6698.

[23] K. A. Modic, T. E. Smidt, I. Kimchi, N. P. Breznay, A. Biffin, S. Choi, R. D. Johnson, R. Coldea, P. Watkins-Curry, G. T. McCandless, J. Y. Chan, F. Gandara, Z. Islam, A. Vishwanath, A. Shekhter, R. D. McDonald, and J. G. Analytis, Nat. Commun. **5**, 4203 (2014).

[24] A. Biffin, R. D. Johnson, I. Kimchi, R. Morris, A. Bombardi, J. G. Analytis, A. Vishwanath, and R. Coldea, Phys. Rev. Lett. **113**, 197201 (2014).

[25] T. Takayama, A. Kato, R. Dinnebier, J. Nuss, H. Kono, L. S. I. Veiga, G. Fabbris, D. Haskel, and H. Takagi, Phys. Rev. Lett. **114**, 077202 (2015).

[26] A. Biffin, R. D. Johnson, S. Choi, F. Freund, S. Manni, A. Bombardi, P. Manuel, P. Gegenwart, and R. Coldea, Phys. Rev. B **90**, 205116 (2014).

[27] Y. Okamoto, M. Nohara, H. Aruga-Katori, and H. Takagi, Phys. Rev. Lett. **99**, 137207 (2007).

[28] I. Kimchi, J. G. Analytis, and A. Vishwanath, Phys. Rev. B **90**, 205126 (2014).

[29] Microscopic exchange pathways for edge-sharing octahedra have been discussed in Refs. [2,3,11,13,30,36,41–44].

[30] G. Khaliullin, Progress Theor. Phys. Suppl. **160**, 155 (2005).

[31] I. Kimchi and A. Vishwanath, Phys. Rev. B **89**, 014414 (2014).

[32] H.-C. Jiang, Z.-C. Gu, X.-L. Qi, and S. Trebst, Phys. Rev. B **83**, 245104 (2011).

[33] M. J. O'Malley, H. Verweij, and P. M. Woodward, J. Solid State Chem. **181**, 1803 (2008).

[34] E. K.-H. Lee and Y. B. Kim, Phys. Rev. B **91**, 064407 (2015).

[35] The a-axis spiral orders discussed in Ref. [34] ("SP$_{a+}$" and "SP$_{a-}$") exhibit features of noncoplanarity and counter-rotation, but have a different symmetry compared to the spiral phase found experimentally in γ-Li$_2$IrO$_3$. The pattern of noncoplanarity of the spiral planes predicted for γ-Li$_2$IrO$_3$ is such that it alternates between successive *pairs* of zigzag chains along c; whereas experimentally it is found that it alternates between consecutive zigzag chains [24], as illustrated in Fig. 3 (bottom right). The order in β-Li$_2$IrO$_3$ is however correctly captured by one of the spiral orders found in that work with sign-flipped Γ interactions, specifically $\bar{S}P_{a-}$. In contrast, here the experimentally determined structures for both the β and the γ polytypes are captured naturally by the KJI minimal model proposed in Eq. (1).

[36] J. G. Rau, E. K.-H. Lee, and H.-Y. Kee, Phys. Rev. Lett. **112**, 077204 (2014).

[37] Y. Yamaji, Y. Nomura, M. Kurita, R. Arita, and M. Imada, Phys. Rev. Lett. **113**, 107201 (2014).

[38] V. M. Katukuri, S. Nishimoto, V. Yushankhai, A. Stoyanova, H. Kandpal, S. Choi, R. Coldea, I. Rousochatzakis, L. Hozoi, and J. van den Brink, New J. Phys. **16**, 013056 (2014).

[39] C. G. Broyden, IMA J. Appl. Math. **6**, 76 (1970).

[40] R. H. Byrd, P. Lu, and J. Nocedal, SIAM J. Sci. Stat. Comput. **16**, 1190 (1995).

[41] G. Chen and L. Balents, Phys. Rev. B **78**, 094403 (2008).

[42] T. Micklitz and M. R. Norman, Phys. Rev. B **81**, 174417 (2010).

[43] M. R. Norman and T. Micklitz, Phys. Rev. B **81**, 024428 (2010).

[44] I. I. Mazin, H. O. Jeschke, K. Foyevtsova, R. Valentí, and D. I. Khomskii, Phys. Rev. Lett. **109**, 197201 (2012).